Electronic Supplementary Material (ESI) for Journal of Materials Chemistry A. This journal is © The Royal Society of Chemistry 2022

Electronic Supplementary Information

for

Structural Engineering of Metal Organic Layers Toward Stable Li-CO_2 Batteries

Zhibin Cheng,*[a,b] Yanlong Fang,[a] Wen Dai,[a] Jindan Zhang,[a] Shengchang Xiang,[a] and Zhangjing Zhang*[a,b]

[a.] *Fujian Key Laboratory of Polymer Materials, College of Chemistry and Materials Science, Fujian Normal University, Fuzhou 350007, China. Email: chengzhibin@fjnu.edu.cn, zzhang@fjnu.edu.cn*

[b.] *State Key Laboratory of Structural Chemistry, Fujian Institute of Research on the Structure of Matter, Chinese Academy of Sciences, Fuzhou, Fujian, 350002, China*

Materials

All starting reagents and solvents were purchased from commercial companies and used without further purification. N,N-Dimethylacetamide (DMA, AR), N,N-dimethylformamide (DMF, AR) was bought from Aladdin Industrial Corporation. $MnCl_2 \cdot 4H_2O$ (99%), $Zn(NO_3)_2 \cdot 4H_2O$ (99%) were purchased from Sinopharm Chemical Reagent Co., Ltd. 1,6,7,12-Tetrachloroperylene tetracarboxylic acid dianhydride (95%) were purchased from Tansoole. The carbon fiber paper were purchased from Phychemi (HK) Company Limited Co., Ltd., the models is GDL280.

Single-crystal X-ray structural analysis

Data collection and structural analysis of crystal Mn-TTA and Zn-TTA were performed on an Agilent Technologies SuperNova single crystal diffractometer equipped with graphite monochromatic Cu Kα radiation (λ = 1.54184 Å). The crystal was kept at 273 K during data collection. Using Olex2, the structure was solved with the Superflipstructure solution program using charge flipping and refined with the ShelXL refinement package using least squares minimization. All nonhydrogen atoms were refined with anisotropic displacement parameters. The hydrogen atoms on the ligands were placed at idealized positions and refined using a riding model. The detailed crystallographic data and structure refinement parameters are summarized in Table S3 (CCDC 2143640, CCDC 2143641).

Structure characterization

Powder X-ray diffraction (PXRD) was carried out with a PANalytical X'Pert powder diffractometer equipped with a Cu-sealed tube (l¼1.541874 Å) at 40 kV and 40 mA over the 2θ range of 5–50°. Thermogravimetric analysis (TGA) was measured at a heating rate of 10 °C min^{-1} using a STA449 C Jupiter thermo gravimetric analyzer (NETZSCH). SEM images were obtained with a JEOL JSM-7500F scanning electron microscope. The samples were sputtered with Au (nano-sized film) prior to imaging. Elemental analyses (C, H and N) were performed on a Perkin-Elmer 240C analyzer. X-ray photoelectron spectroscopy (XPS)

measurements were conducted on a VG Scientific ESCA Lab Mark II spectrometer using Al Kα as the X-ray source. The pass energy for survey spectra and high-resolution spectra and are 100.0 eV and 20.0 eV, respectively. Energy step size for survey spectra and high-resolution spectra are 1.0 eV and 0.1 eV, respectively. All binding energies were referenced to the C 1s peak of the surface adventitious carbon at 284.8 eV. Inductively coupled plasma (ICP) analysis was performed on an PerkinElmer Optima 8000. Fourier transform infrared spectra (FT-IR, ATR) were measured in the range of 400-4000 cm^{-1} by a Nicolet 5700 FT-IR. A Micromeritics ASAP 2020 surface area analyzer was used to measure the gas adsorption. Raman spectra were measured in the range of 400-3000 cm^{-1} by a Raman-Xplora (XploRA PLUS, HORIBA Jobin Yvon, France).

Electrochemical Characterization

Electrochemical experiments were performed via CR2032 coin-type test cells assembled with lithium metal as the counter and reference electrode in an argon-filled glovebox, where the moisture and oxygen levels were both kept below 1.0 ppm. glass fiber separator (18 mm in diameter) was used as the separator. 1 M LiTFSI dissolved in TEGDME solution was chosen as the electrolyte for all Li-CO_2 batteries and the amount of electrolyte used is 0.5 mL. The electrode was cut into circular pieces with 7 mm radius, and the areal mass loading of catalysts was ~0.35 mg cm^{-2}. Six hole (2 mm in diameter) was drilled in the cathode shell so that the CO_2 can easily and quickly accesses the cathode. Then, the assembled batteries were placed in a 500 mL glass vessel filled with high-purity CO_2. The pure CO_2 was pumped into the glass vessel through the straight two-way piston conducted alternatively by vacuuming and ventilating three times. Before testing, the cells were aged for 24 h. The discharge/charge measurements were conducted at a voltage interval of 2.0 to 4.5 V using a Neware battery test system (Neware Technology Co., Ltd.). Cyclic voltammetry (CV) and electrochemical impedance spectroscopy (EIS) measurements were performed on CHI604E electrochemical workstation. The CV scan rate was fixed at 0.1 mV s^{-1}, 0.2 mV s^{-1} and EIS was measured with

an applied sinusoidal excitation voltage of 5 mV in the frequency range from 100 kHz to 0.1 Hz. All potentials were referenced against Li/Li^+.

Conductivity Measurement

Electronic conductivity was evaluated by the measurement of $I-V$ curves at the probe station with a Keithley 4200 semiconductor characterization system in voltage-sweeping mode. The fresh sample was ground and pressed into 2 mm diameter pellets using a manual tablet press at the pressure of 0.26 T. The thickness of the pellet was measured by micrometer (Mn-TTA: L = 1 mm; Zn-TTA: L = 0.6 mm). Silver paste was used to connect the pellet samples to the electode probes. Direct current two terminal method were investigated its conductivity with an input voltage -30 to 30 V and a sweep rate of 100 mV/s. The electronic conductivity was calculated via the following equation:

$$\sigma = \frac{l}{RS}$$

where l and S are the length (cm) and cross-sectional area (cm^2) of the samples, respectively, and R, which was extracted directly from the impedance plots, is the bulk resistance of the sample (V).

ICP-OES Measurements

1 mg of Cr/Mn-TTA MOL was suspended in nitric acid (3 M, 20 mL). The mixture was ultrasonicated continuously for 10 min to form a uniform suspension. The suspension was left to stand for 12 h at room temperature and then filtered through a filter of size 0.22 μm to obtain a clarified solution. A volume of 4 ml of the filtrate was diluted with deionised water to make a 10 ml solution for the test. Three parallel measurements were carried out for each sample.

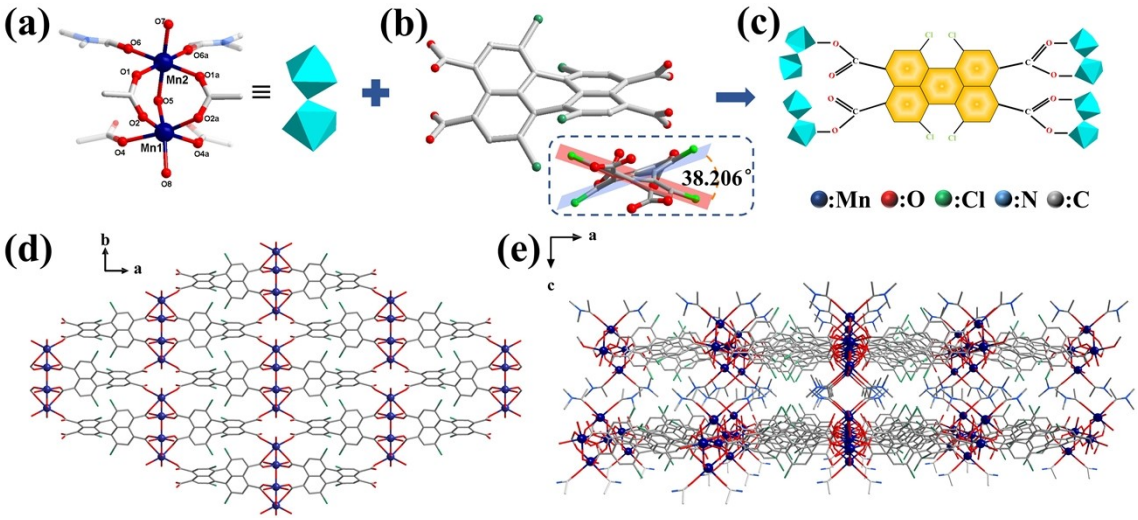

Fig. S1. (a) The structures of Mn-TTA showing: the coordination environment of Mn(II) ion; (b) Organic ligand TTA and the twist angle between the naphthalene; (c) The coordination mode of the $[Mn_2O(COO)_4(DMA)_2(H_2O)_2]$ and TTA; (d) Formation of the 2D coordination layer from 4-linked SBUs and 4-linked TTA ligands; (e) Stacked form of the Mn-TTA two-dimensional layer.

Table S1. The value of the bond valence sums (*Vi*) for Mn-TTA (Mn1，Mn2).

Bond	d_{ij} **(Å)**	V_{ij}	**Bond**	d_{ij} **(Å)**	V_{ij}
Mn(1)-O(8)	2.148	0.244	Mn(2)-O(5)	2.170	0.330
Mn(1)-O(4)	2.230	0.273	Mn(2)-O(1)	2.174	0.327
Mn(1)-O(2)	2.159	0.340	Mn(2)-O(6)	2.125	0.373
Mn(1)-O(4a)	2.230	0.255	Mn(2)-O(6a)	2.125	0.373
Mn(1)-O(5)	2.265	0.273	Mn(2)-O(1a)	2.174	0.327
Mn(1)-O(2a)	2.159	0.340	Mn(2)-O(7)	2.165	0.336
		V_{i1}=1.725			V_{i2}=2.066

Here the valence $V_{ij} = \exp[\frac{R_0 - d_{ij}}{B}]$ and $V_i = \pm \sum_j V_{ij}$, d_{ij} is the bond length between the two ions. R_0 is the reference bond length with 1.76 Å for the Mn-O bond and B is a constant approximately equal to 0.37.[1]

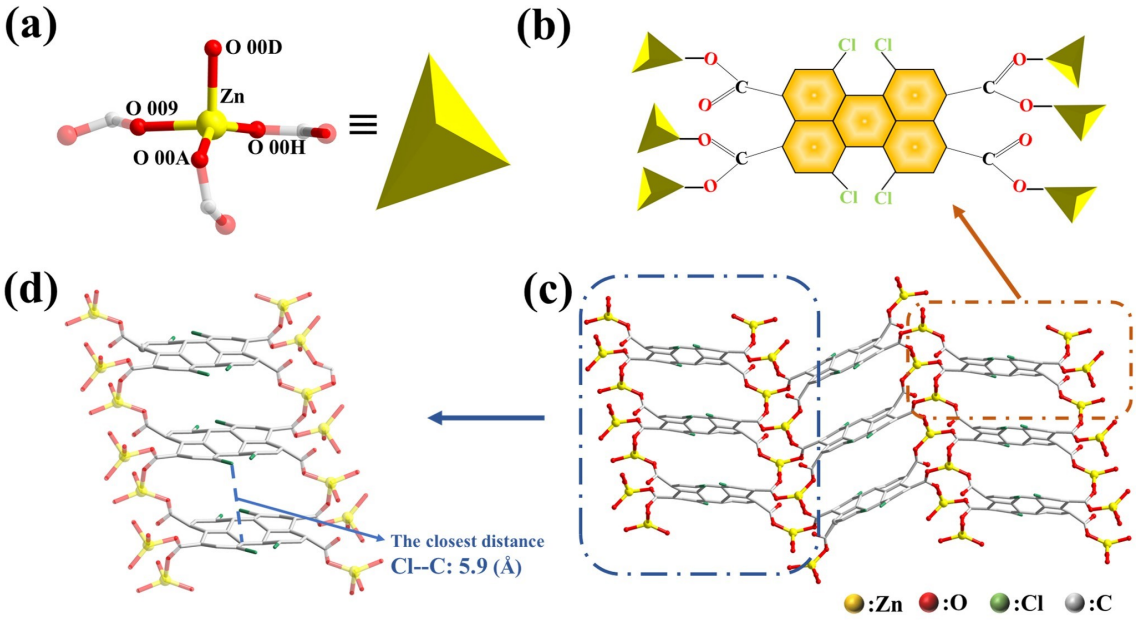

Fig. S2. (a) The structures of Zn-TTA(a–c) showing: the coordination environment of Zn(II) ion; (b) The coordination mode of the [Zn $(COO)_3$ (H_2O)] and TTA; (c) Formation of the 2D coordination layer from 6-connected SBUs and 3-connected TTA ligands; (d) The TTA molecules connecting adjacent metal-oxide networks to form a ladder-type network (blue dotted line: intermolecular lone pair-π interaction).

Bright yellow block crystals of Mn-TTA were obtained by solvothermal reaction of TTA and $Zn(NO_3)_2 \cdot 6H_2O$ in DMA/H_2O mixed solution at 80°C for 48 h. The single-crystal X-ray diffraction analysis showed Zn-TTA belongs to the monoclinic space group *I2/a*, unit cell parameters is a=22.732(2) Å, b=6.1027(4) Å, c=27.0602(12) Å; α=γ=90°, β=99.429(6)°. The asymmetric basic unit of Zn-TTA consists of 1/2 TTA molecules, one Zn (II) and coordination water molecules. All Zn (II) are tetra-coordinated and have a twisted tetrahedral [Zn-O] geometry, formed by oxygen atoms on carboxylic acids from three TTA and one oxygen atom on a water molecule. [Zn-O] has a bond length of 1.874 Å. [Zn-O] forms a one-dimensional [Zn-O] chain by contributing carboxylic acids on TTA molecules, and due to the twisting of the central aromatic ring, the [Zn-O] chain forms an infinite two-dimensional band with "folds" when bridged through the TTA. Due to the twisting of the central aromatic ring, the [Zn-O] chain forms an infinite two-dimensional band with "folds" when bridged by TTA.

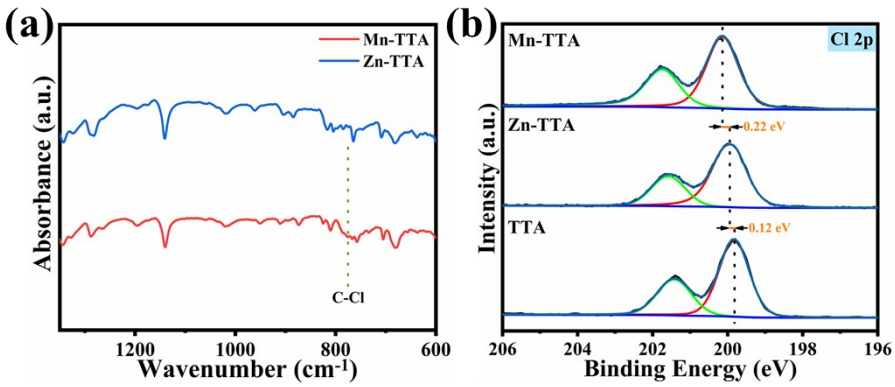

Figure S3. (a) Infrared spectrum and (b) Cl 2p XPS spectra of Zn-TTA and Mn-TTA.

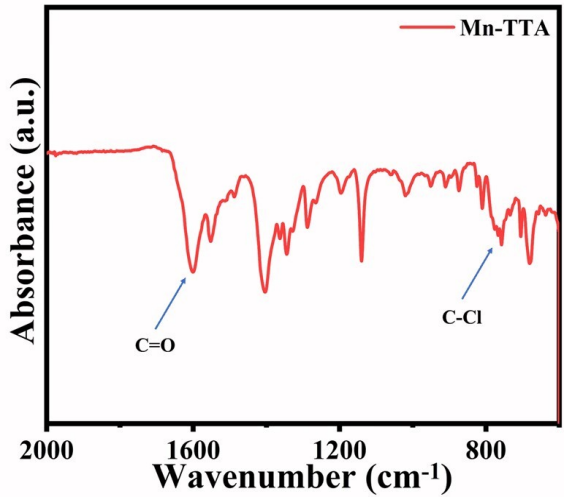

Fig. S4. Infrared spectrum of Mn-TTA.

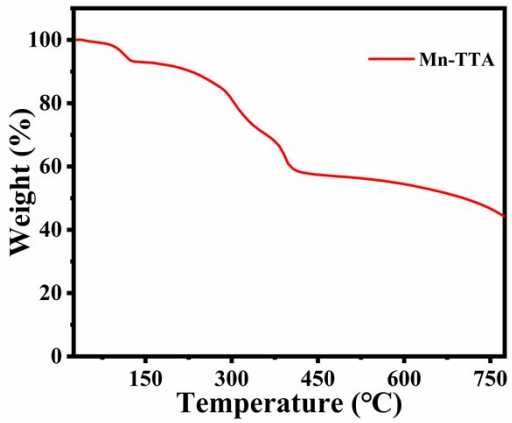

Fig. S5. TGA curve of Mn-TTA.

In TGA curve of Mn-TTA (Fig. S5), the initial weigh loss at the first stage is assigned to the removal of coordination solvent molecules. And the escape of coordination solvent could

induce Mn-TTA MOL to expose more unsaturated coordination of the Mn active catalytic site, which is favourable for the chemisorption and catalytic conversion of CO_2.

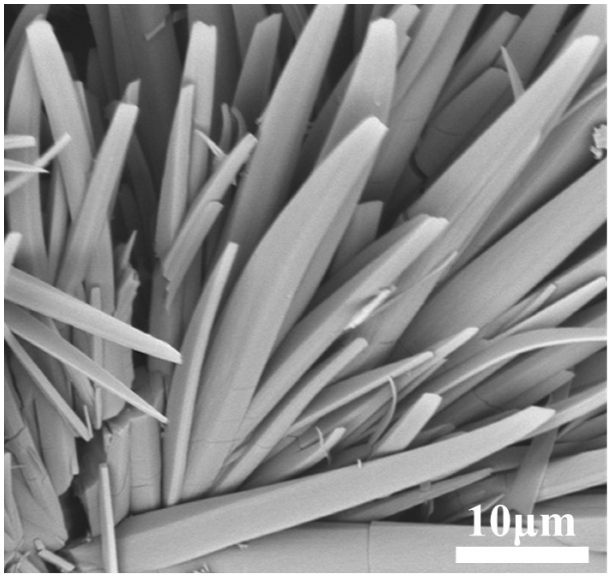

Fig. S6. SEM image of Mn-TTA MOF grown in situ on carbon paper.

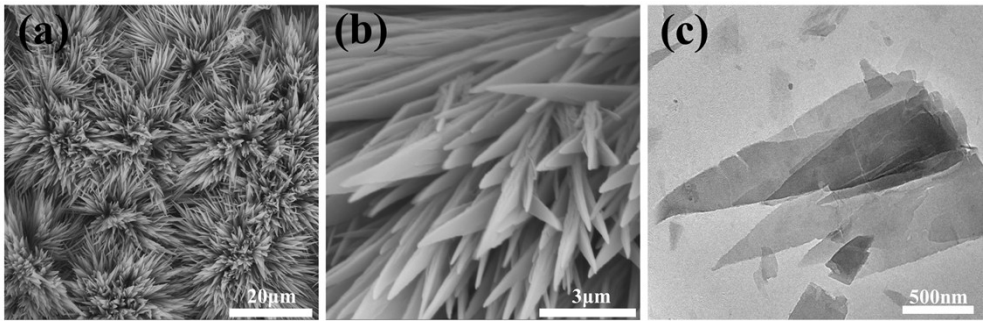

Fig. S7. (a,b) SEM image for Mn-TTA MOL; (c) TEM image for Mn-TTA MOL.

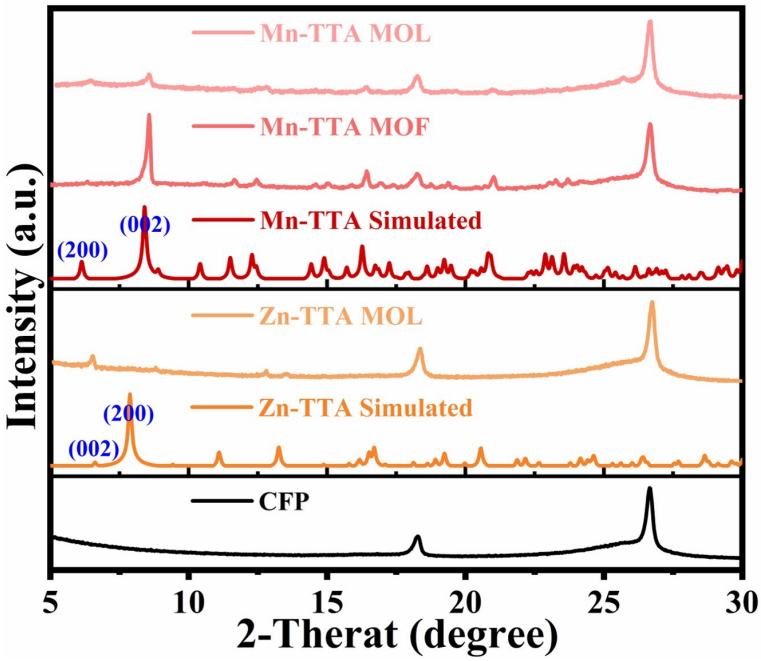

Fig. S8. The powder X-ray diffraction patterns of Mn-TTA and Zn-TTA.

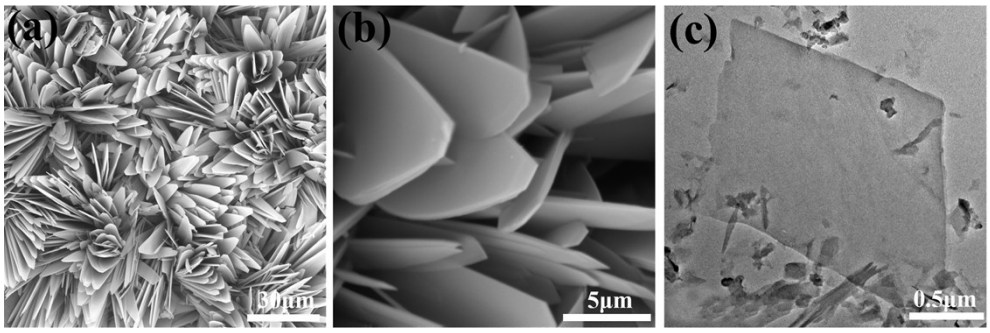

Fig. S9. (a,b) SEM image for Zn-TTA MOL; (c) TEM image for Zn-TTA MOL.

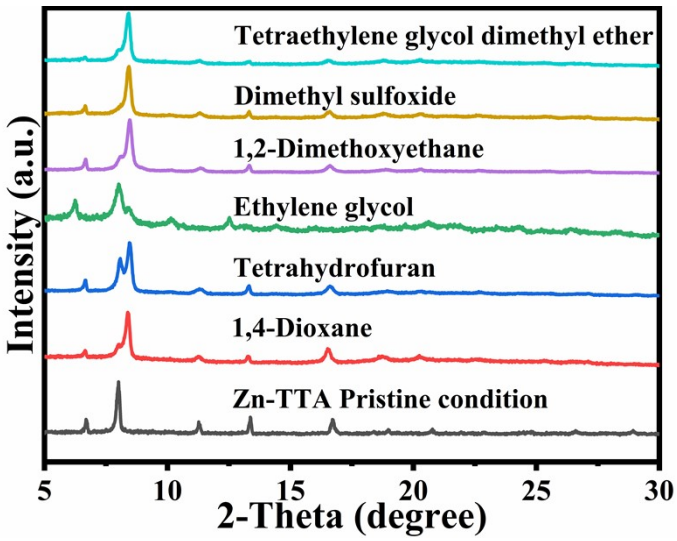

Fig. S10. Stability test results of Zn-TTA incubated in various solvents for 24 hours.

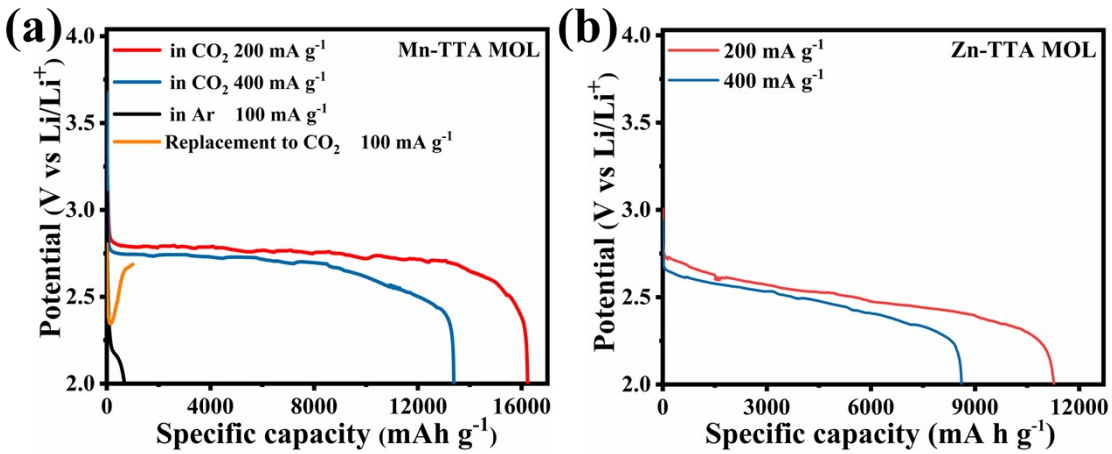

Fig. S11. Discharge voltage curves of (a) Mn-TTA MOL under CO_2 or Ar, and (b) Zn-TTA MOL under CO_2 with different current densities.

The Mn-TTA MOL electrode exhibited an extremely low discharge capacity in Ar. However, after replacing Ar with CO_2, the discharge voltage gradually increased to normal levels, the test results further validating the role of CO_2. The full discharge capacities of Mn-TTA MOL were 16233.4 and 13388.1 mAh g^{-1} at the current density of 200 mA g^{-1} and 400 mA g^{-1}, respectively. (Fig. S11a) By contrast, the full discharge capacities of Zn-TTA MOL were 11281.7 and 8622.64 mAh g^{-1} at the current density of 200 mA g^{-1} and 400 mA g^{-1}, respectively. (Fig. S11b). This result further indicated that Zn-TTA MOL possesses the better catalytic activity for boosting CO_2 conversion.

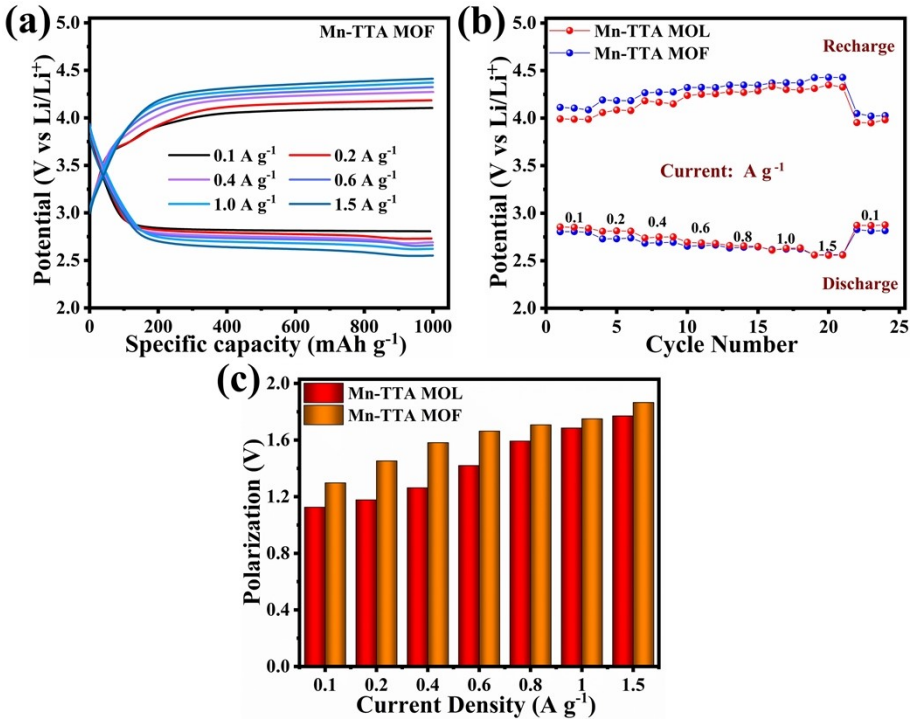

Fig. S12. (a) Discharge/charge curves and (b) rate performance of the Mn-TTA MOF and Mn-TTA MOL electrode under a limited capacity of 1000 mAh g^{-1} at different current densities. (c) Battery overpotentials at various current densities.

In order to better demonstrate the advantages of 2D Mn-TTA nanosheets, Mn-TTA MOF electrodes were prepared. As shown in Figurs S12a, both Mn-TTA MOF and Mn-TTA MOL electrodes are able to alleviate the severe polarization voltage in high stress cycles, but the polarization voltage of Mn-TTA MOF electrode is still slightly larger than that of Mn-TTA MOL at different current densities (Figure S12b). Mn-TTA nanosheets with ultrathin dimensions proved to have better catalytic activity than their MOF native counterparts in electrocatalysis due to the increased exposure of catalytic sites as well as weakened mass transfer limitations.

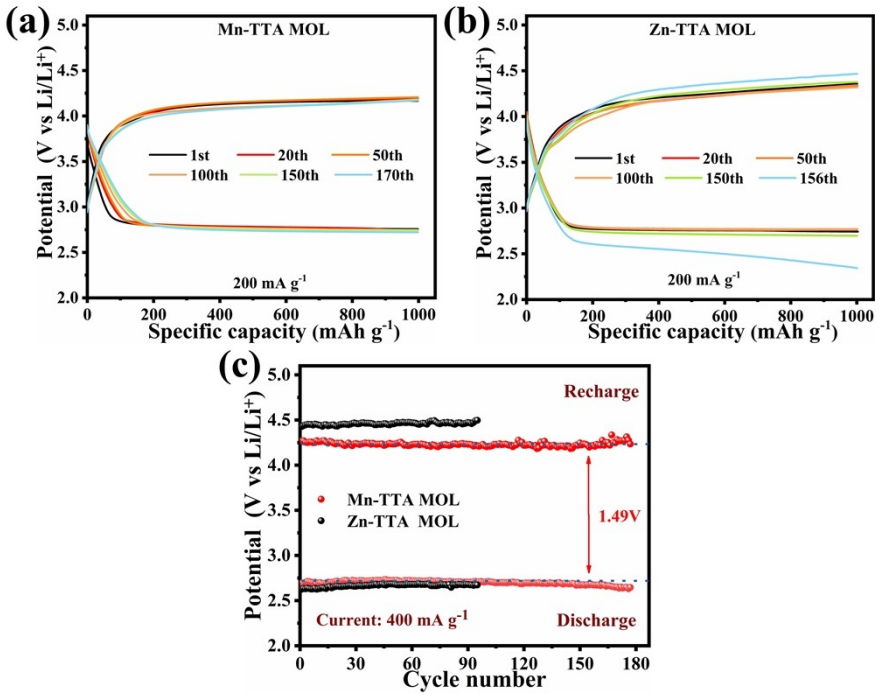

Fig. S13. (a,b) Cycle properties of the Mn-TTA MOL and Zn-TTA MOL cathode at 200 mA g^{-1} and (c) 400 mA g^{-1} with a limited capacity of 1000 mAh g^{-1}, respectively.

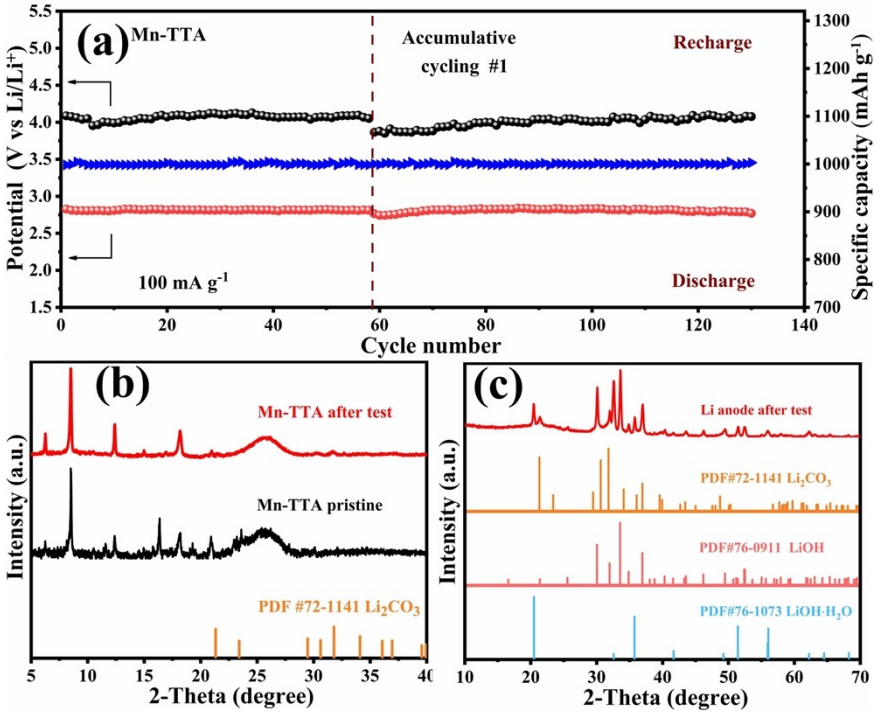

Fig. S14. (a) Cycling performance of the bulky Mn-TTA cathode at 100 mA g^{-1} with a limited capacity of 1000 mAh g^{-1}, (b,c) XRD patterns of the retrieved Mn-TTA/CFP cathode and Li anode.

The cycled Mn-TTA cathode was assembled in a Li-CO_2 cell with fresh Li anode and electrolyte. This reassembled cell provided similar electrochemical performance to the initial cell, which continued to operate stably for 70 cycles at a current density of 100 mA g^{-1} (Fig. S14a). Previous studies suggested that the undecomposed Li_2CO_3 gradually accumulated on active sites of the catalyst, thereby causing the overpotential to rise with cycles and eventually contributing to the Li-CO_2 battery malfunction. Nevertheless, the XRD pattern of the spent Mn-TTA/CFP electrode still showed a strong Mn-TTA (002) crystalline feature peak and a weaker Li_2CO_3 feature peak, indicating that the Mn-TTA has good structural stability and the better catalytic activity avoids the excessive deposition of reaction products on its surface (Fig. S14b). However, the presence of high levels of discharge products in the lithium anode suggests that accumulated discharge products corroding the lithium anode are the main cause of battery failure (Mn-TTA/CFP cathode reveals that inconspicuous Li_2CO_3 residue was observed in the present work, and the Mn-TTA retains the characteristic peaks of its structure after up to two months of cyclic test in Fig. S14c). Through a series of experiments, we have demonstrated that the Mn-TTA material maintains its catalytic activity during cycling regardless of the failure of the lithium anode and electrolyte state.

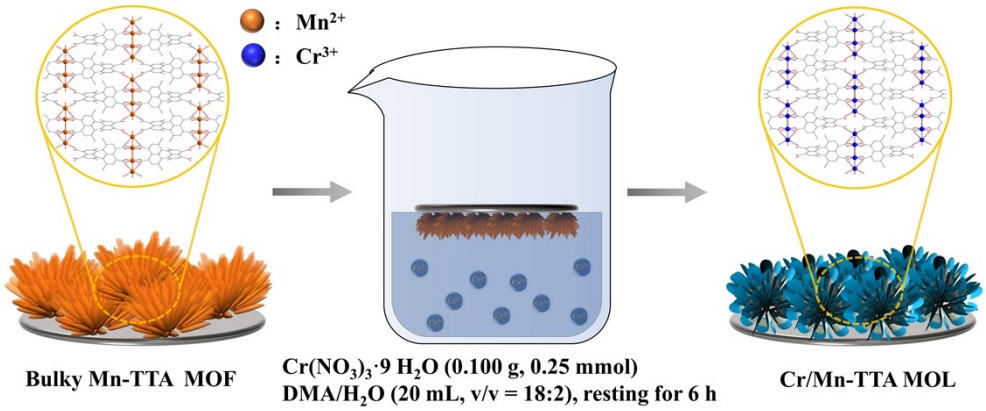

Fig. S15. Schematic diagram of ion exchange.

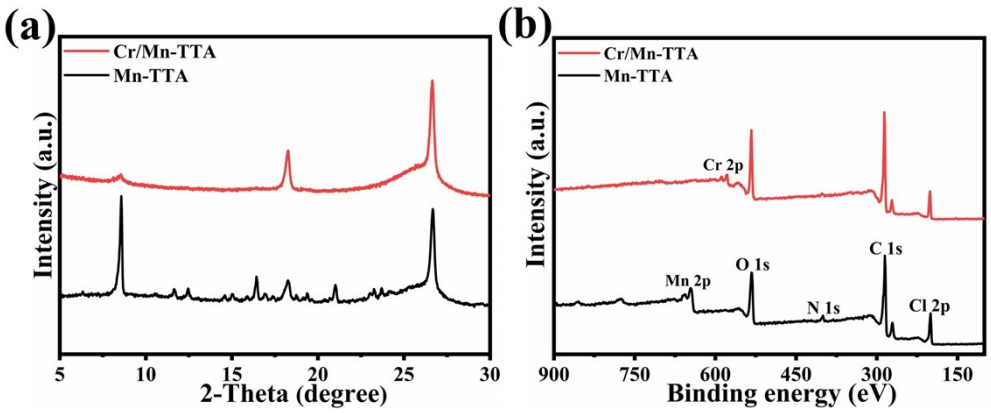

Fig. S16. (a) XRD and (b) XPS patterns for bulky Mn-TTA MOF, Cr/Mn-TTA MOL.

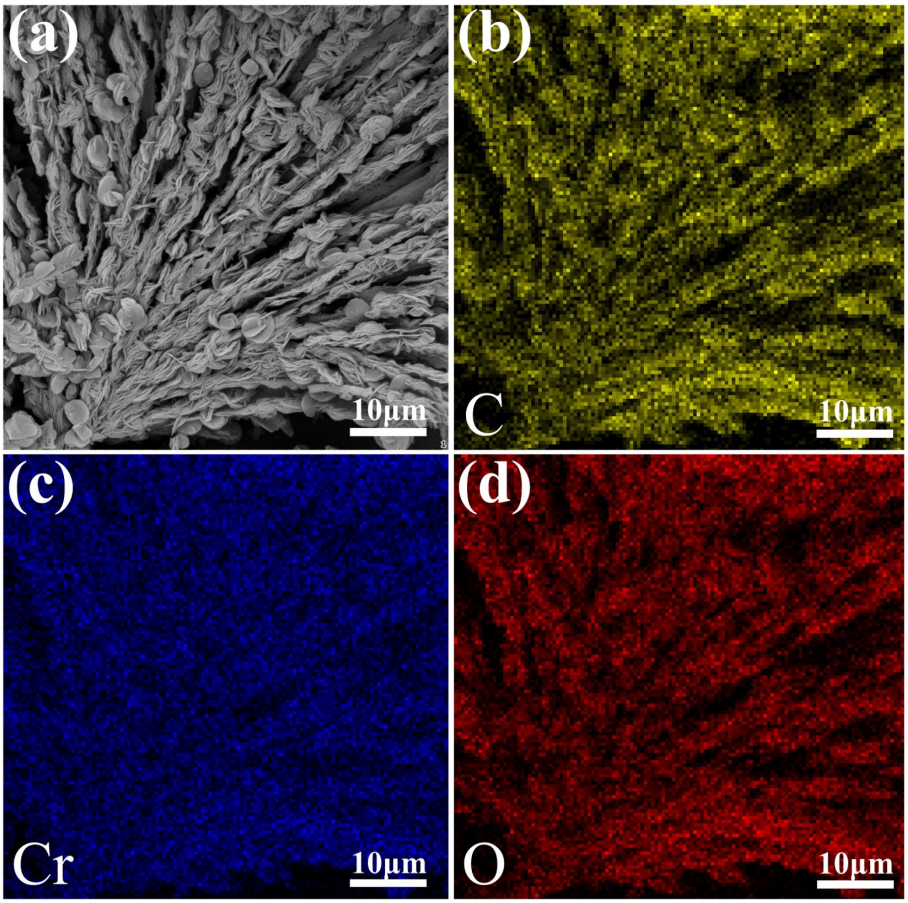

Fig. S17. (a) SEM and (c-d) EDS patterns for Cr/Mn-TTA MOL.

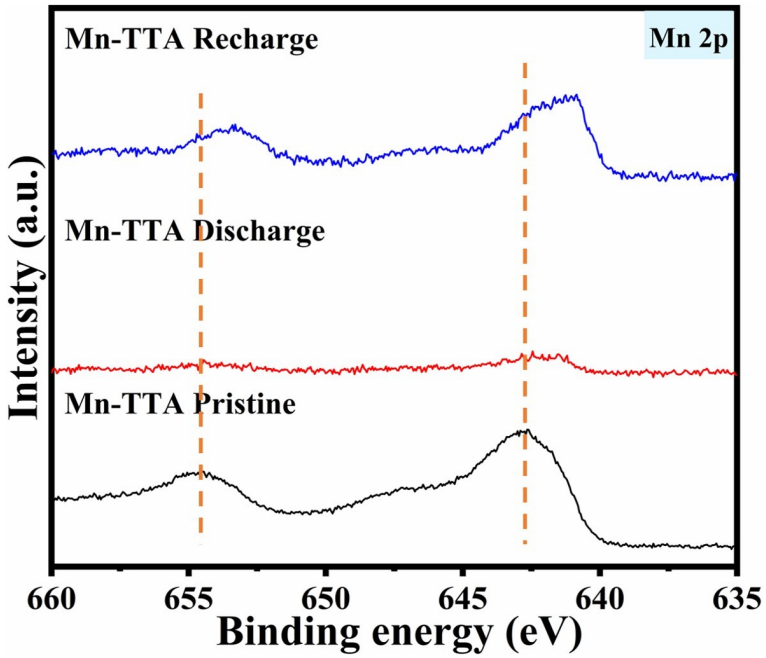

Fig. S18. XPS Mn 2p spectra of Mn-TTA/CFP cathode before tested, after discharge and recharge.

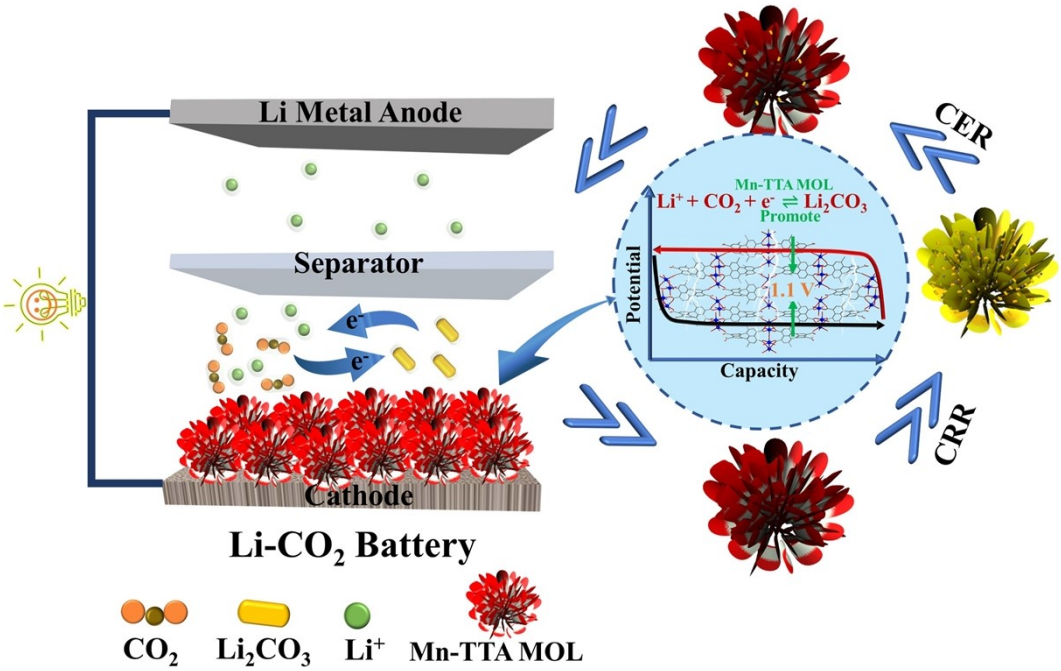

Fig. S19. Schematic cell configuration of the Mn-TTA MOL with catalytic effects toward CO_2.

Table S2. Comparison of electrochemical performances of Li-CO_2 batteries with different cathodes.

Catalyst	Capacity/Current (mAh g^{-1}/ mA g^{-1})	Cycle number	Capacity (mAh g^{-1})	Polarization (V)	Cycle life at high current densities	References
$Co_{0.2}Mn_{0.8}O_2$ /CC	1000/100	500	8203 (100 mA g^{-1})	0.73	45 (500 mA g^{-1})	2
Mn_2(dobdc) /CNT	1000/50	30	18022 (50 mA g^{-1})	1.65	50 (200 mA g^{-1})	3
MnTPzP-Mn	1000/100	50	14025 (100 mA g^{-1})	1.05	90 (200 mA g^{-1})	4
Ru/ACNFs	1000/100	50	11495 (100 mA g^{-1})	1.53	--	5
Ni-NG	1000/100	101	17625 (100 mA g^{-1})	1.43	18 (200 mA g^{-1})	6
Ni-rGO	1000/100	100	8991 (100 mA g^{-1})	1.05	--	7
CNT@ 2.5MnO_2	1000/200	50	9200 (100 mA g^{-1})	1.28	--	8
3D NCNT/G	1000/100	185	17534 (100 mA g^{-1})	1.13	--	9
TDG-1000	500/100	600	70000 (100 mA g^{-1})	1.12	230 (1000 mA g^{-1})	10
Ru/Co-CPY@CNT	1000/500	180	24740 (200 mA g^{-1})	1.05	--	11
MnO@ NC-G	1000/50	20	25021 (50 mA g^{-1})	0.88	200 (1000 mA g^{-1})	12
COF-Ru@CNT	1000/400	150	27348 (100 mA g^{-1})	1.24	200 (1000 mA g^{-1})	13
Graphene@COF	500/500	56	27833 (75 mA g^{-1})	1.08	56 (500 mA g^{-1})	14
NH_2-Cu-MOFs@RuO_2	100 μA h cm^{-2} / 50 μA cm^{-2}	140	2903.3 μA h cm^{-2} (50 μA cm^{-2})	1.21		15
CoPc–Mn–O	0.2 mA h cm^{-2} / 0.2 mA cm^{-2}	30		0.05 (0.01 mA/cm^{-2})	60 h (0.02 mA/cm^{-2})	16
TTCOF-Mn	1000/300	180	13018 (100 mA g^{-1})	1.07	180 (300 mA g^{-1})	17
Mn-TTA	1000/100	70	22229	1.11	This work	
	1000/200	170	16233	1.25		
	1000/400	170	13388	1.44		
	1000/1000	300		1.67		
Zn-TTA	1000/100	95	18826.9	1.56	This work	
	1000/200	156	11281.7	1.67		
	1000/400	95	8622.6	1.79		

Table S3. Crystal data and structure refinement for Mn-TTA and Zn-TTA.

	Mn-TTA	**Zn-TTA**
CCDC	2143641	2143640
Crystal system	Orthorhombic	Monoclinic
Space group	*Cmce*	*I2/a*
a/Å	28.8094(18)	22.732(2)
b/Å	12.2544(8)	6.1027(4)
c/Å	21.0312(17)	27.0602(12)
α/°	90	90
β/	90	99.429 (6)
γ/°	90	90
Volume/Å^3	7424.9(9)	3703.2(5)
Z	8	4
ρ_{calc}g/cm^3	1.6034	1.307
F(000)	3628.1	1440.0
Radiation	Mo Kα (λ = 0.710)	Cu Kα (λ = 1.54184)
Goodness-of-fit on F^2	1.065	1.086
Final R indexes [all data][(a)]	R1 = 0.0775, wR2 = 0.1815	R1 = 0.1200, wR2 = 0.2817

References

1. Q. Song, Y. Yang, F. Yuan, S. Zhu, J. Wang, S. Xiang and Z. Zhang, *J. Mater. Chem. A*, 2022, **10**, 9363-9369.
2. B. Ge, Y. Sun, J. Guo, X. Yan, C. Fernandez and Q. Peng, *Small*, 2019, **15**, 1902220.
3. S. Li, Y. Dong, J. Zhou, Y. Liu, J. Wang, X. Gao, Y. Han, P. Qi and B. Wang, *Energy Environ. Sci.*, 2018, **11**, 1318-1325.
4. L. Z. Dong, Y. Zhang, Y. F. Lu, L. Zhang, X. Huang, J. H. Wang, J. Liu, S. L. Li and Y. Q. Lan, *Chem. Commun.*, 2021, **57**, 8937-8940.
5. Y. Qiao, S. Xu, Y. Liu, J. Dai, H. Xie, Y. Yao, X. Mu, C. Chen, D. J. Kline, E. M. Hitz, B. Liu, J. Song, P. He, M. R. Zachariah and L. Hu, *Energy Environ. Sci.*, 2019, **12**, 1100-1107.
6. Z. Zhang, X. G. Wang, X. Zhang, Z. Xie, Y. N. Chen, L. Ma, Z. Peng and Z. Zhou, *Adv. Sci.*, 2018, **5**, 1700567.

7. Y. Qiao, Y. Liu, C. Chen, H. Xie, Y. Yao, S. He, W. Ping, B. Liu and L. Hu, *Adv. Funct. Mater.*, 2018, **28**, 1805899.
8. Q. Liu, Z. Hu, L. Li, W. Li, C. Zou, H. Jin, S. Wang and S. L. Chou, *ACS Appl. Mater. Interfaces*, 2021, **13**, 16585-16593.
9. Y. Xiao, F. Du, C. Hu, Y. Ding, Z. Wang, A. Roy and L. Dai, *ACS Energy Lett.*, 2020, **5**, 916-921.
10. F. Ye, L. Gong, Y. Long, S. Talapaneni, L. Zhang, Y. Xiao, D. Liu, C. Hu and L. Dai, *Adv. Energy Mater.*, 2021, **11**, 2101390.
11. J.-H. Wang, Y. Zhang, M. Liu, G.-K. Gao, W. Ji, C. Jiang, X. Huang, Y. Chen, S.-L. Li and Y.-Q. Lan, *Cell Rep. Phys. Sci.*, 2021, **2**, 100583.
12. S. Li, Y. Liu, J. Zhou, S. Hong, Y. Dong, J. Wang, X. Gao, P. Qi, Y. Han and B. Wang, *Energy Environ. Sci.*, 2019, **12**, 1046-1054.
13. X. Li, H. Wang, Z. Chen, H. S. Xu, W. Yu, C. Liu, X. Wang, K. Zhang, K. Xie and K. P. Loh, *Adv. Mater.*, 2019, **31**, 1905879.
14. S. Huang, D. Chen, C. Meng, S. Wang, S. Ren, D. Han, M. Xiao, L. Sun and Y. Meng, *Small*, 2019, **15**, 1904830.
15. H. Hong, J. He, Y. Wang, X. Guo, X. Zhao, X. Wang, C. Zhi, H. Li and C. Han, *J. Mater. Chem. A,*, 2022, **10**, 18396–18407.
16. J. Wang, S. Li, Y. Chen, L. Dong, M. Liu, J. Shi, S. Li and Y. Lan, *Adv. Funct. Mater*, 2022, **32**, 2210259.
17. Y. Zhang, R. Zhong, M. Lu, J. Wang, C. Jiang, G. Gao, L. Dong, Y. Chen, S. L. Li and Y. Lan, *ACS Cent. Sci.*, 2021, **7**, 175-182.